ELSEVIER

On the origin of kinking in layered crystalline solids

G. Plummer [1], H. Rathod [2], A. Srivastava [2], M. Radovic [2], T. Ouisse [3], M. Yildizhan [4], P.O.Å. Persson [4], K. Lambrinou [5,6], M.W. Barsoum [7,*], G.J. Tucker [1,*]

[1] Department of Mechanical Engineering, Colorado School of Mines, Golden, CO 80401, USA
[2] Department of Materials Science and Engineering, Texas A&M University, College Station, TX 77840, USA
[3] Université Grenoble Alpes, CNRS, Grenoble INP, LMGP, F-38000 Grenoble, France
[4] Thin Film Physics, Department of Physics, Chemistry and Biology, Linköping University, SE-581 83 Linköping, Sweden
[5] SCK CEN, Boeretang 200, B-2400 Mol, Belgium
[6] School of Computing and Engineering, University of Huddersfield, Queensgate, Huddersfield HD1 3DH, UK
[7] Department of Materials Science and Engineering, Drexel University, Philadelphia, PA 19104, USA

Kinking is a deformation mechanism ubiquitous to layered systems, ranging from the nanometer scale in layered crystalline solids, to the kilometer scale in geological formations. Herein, we demonstrate its origins in the former through multiscale experiments and atomistic simulations. When compressively loaded parallel to their basal planes, layered crystalline solids first buckle elastically, then nucleate atomic-scale, highly stressed ripplocation boundaries – a process driven by redistributing strain from energetically expensive in-plane bonds to cheaper out-of-plane bonds. The consequences are far reaching as the unique mechanical properties of layered crystalline solids are highly dependent upon their ability to deform by kinking. Moreover, the compressive strength of numerous natural and engineered layered systems depends upon the ease of kinking or lack there of.

Introduction

Kinking, a deformation mechanism in which a region buckles and undergoes a uniform rotation to accommodate compressive strain, is ubiquitous in nature and occurs in a variety of natural and engineering materials. These include graphite, mica, ice, wood, laminated composites, and geological formations, spanning over 13 orders of magnitude in scale from nanometers to tens of kilometers. A kink band is confined by two kink boundaries (KBs) and typically assumes a stove pipe configuration (left inset Fig. 1a). At this time, it is fairly well-established that buckling causes the nucleation and growth of kink bands. Historically, the latter were investigated in different communities with little crosstalk between them. More recently, some mechanistic commonalities of kink band formation in various layered systems – e.g., geology and polymer composites – have been appreciated [1]. One of the earliest mentions of kink bands was in 1898 by Mugge, who explored kinking and twinning in a large number of minerals [2]. The formation of kink bands in metals, however, was first reported in 1942 by Orowan, for cadmium single crystals compressed parallel to the basal planes [3]. He postulated that kink bands form by a mechanism where a stack of basal planes snaps abruptly to a tilted position, separated from the unkinked crystal by two KBs. In 1949, Hess and Barrett reproduced Orowan's experiments on zinc [4] and postulated that elastic buckling can produce two oppositely signed dislocation walls, or KBs. Crucially, they did not present more than a schematic for their mechanism. In 1952, Frank and Stroh proposed the first, and to date only, theoretical model of KB formation [5], according to which a pre-kinked nucleus facilitates the generation of dislocations that glide apart into oppositely signed dislocation walls or KBs.

* Corresponding authors.
E-mail addresses: Barsoum, M.W. (barsoumw@drexel.edu), Tucker, G.J. (tucker@mines.edu).

https://doi.org/10.1016/j.mattod.2020.11.014

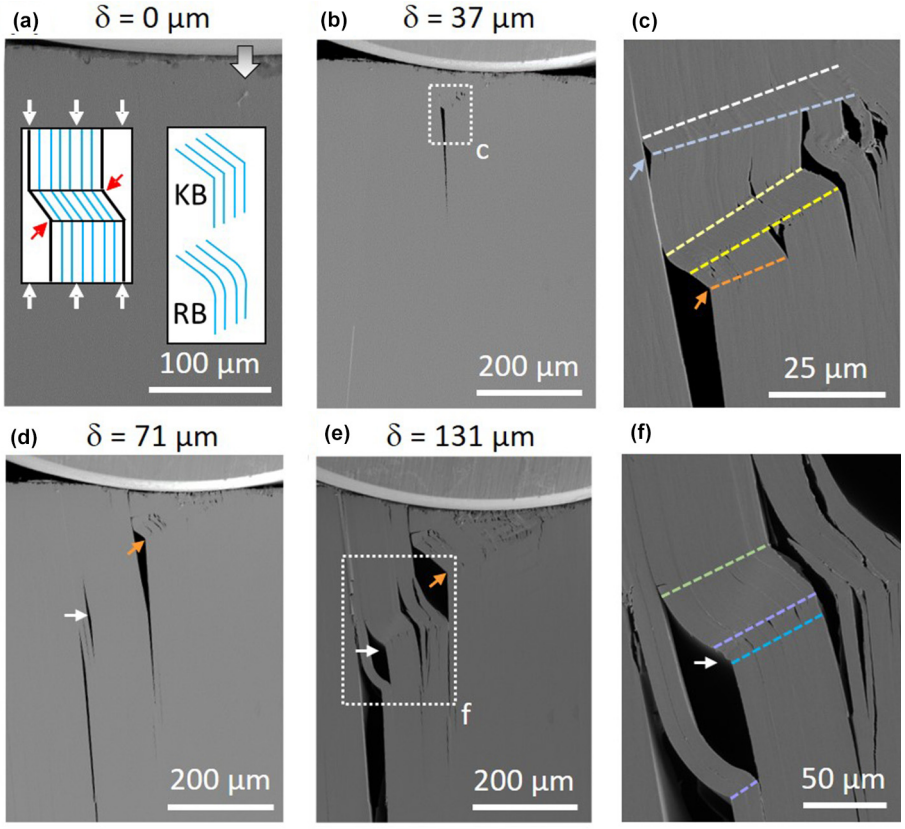

FIGURE 1

In situ SEM indentation of a Cr_2AlC single crystal. (a) Indenter making contact with specimen. Vertical arrow indicates compression direction. Left inset depicts a typical kink band bounded by two KBs; right inset compares KBs and RBs. (b and c) First set of delamination cracks parallel to basal planes and RBs directly beneath indenter. (d) New delamination cracks slightly bridged by ligaments. (e and f) Ligaments between delamination cracks form large-scale RBs. Horizontal arrows in (c—f) mark delamination cracks; dashed colored lines in (c) and (f) indicate RBs. Values of δ denote indentation depths.

What renders this puzzle more intriguing is the fact that many layered crystalline solids (LCSs) can form ripplocations– i.e., atomic-scale ripples in the basal planes – when the basal planes are compressed edge-on [6–11]. Ripplocations in LCSs manifest themselves as ripplocation boundaries (RBs), where a collection of ripplocations self-align into boundaries. The latter are: (i) reversible as long as they are not pinned, (ii) delaminate in regions of maximum curvature as their angle increases, (iii) in contrast to KBs, not atomically sharp (right inset Fig. 1a), and (iv) transformable into KBs under extremes strains. We observe both types of boundaries in experiments and modelling. Previous observations of neatly aligned dislocation walls have been made in graphite [12], mica [13], the MAX phases [14,15], and other LCSs [16,17]. While lower resolution images give the appearance that these boundaries are atomically sharp KBs, more recent atomic resolution images [15,17] suggest the majority are in fact curved RBs (see Fig. S1 for typical examples of both).

Herein, we resolve this hundred-plus-year-old puzzle using the $M_{n+1}AX_n$ (MAX) phases as model materials. We do so by combining multiscale experimental findings with atomistic simulations. The MAX phases – where M is an early transition metal, A is mostly an element from groups 13–16, X is carbon (C) and/or nitrogen (N), and $n = 1–4$ – are best described as thermodynamically stable, metallically bonded nanolaminates. Basal slip is the only operative slip system, and being layered, their propensity to deform by kinking is high [18,19].

This work combines the findings of initially independent efforts. These efforts comprised the *in situ* deformation of Cr_2AlC single crystals in a scanning electron microscope (SEM), the investigation by scanning transmission electron microscope (STEM) of the deformation of single Zr_2AlC grains, and the use of a newly developed Ti_3AlC_2 interatomic potential to computationally model the MAX phases' deformation. Given the similarities in the deformation of all MAX phases [19], it is unlikely that any of the general conclusions reached herein strongly depend on the exact MAX phase composition or stacking. The fact that the conclusions reached complement each other as well as they do can be taken as indirect evidence of their universality.

Material and methods

MAX phase synthesis

Cr_2AlC single crystals were synthesized using a flux growth method in an induction-heated Al_2O_3 crucible based in part on previous work [20]. Flux composition was $X_{Cr} = 0.354$, $X_{Al} = 0.566$, and $X_C = 0.08$. C was introduced at 1650 °C by dipping a rotating graphite rod into the flux. This allowed for precise control of the carbon content and prevented unwanted Al_4C_3

formation and subsequent breaking of the crucible during temperature ramping. After 30 min, the temperature was decreased to 1600 °C in 20 min. Then nucleation and crystal growth were achieved by slow cooling to 1100 °C over 5 days. Crystals were extracted from the solidified flux by HCl etching (see Fig. S2 for phase identification). Zr_2AlC polycrystals were synthesized by means of reactive hot pressing a ZrH_2, Al, and C powder mixture, according to a procedure described elsewhere [21]. The Zr_2AlC polycrystalline ceramic used in this work was hot pressed at 1525 °C and consisted of 67 wt.% Zr_2AlC and 33 wt.% ZrC (see Fig. S3 for phase identification).

Single crystal and grain indentations

The mechanical behavior of single crystal Cr_2AlC was characterized by indentation inside a SEM. A single crystal Cr_2AlC specimen with dimensions $6 \times 6 \times 1.5$ mm^3 was mounted in epoxy to avoid any delamination of layers during specimen preparation. Mechanical machining was carried out using a 3241 model Well Vertical Precision Diamond wire saw. With minimal cutting speed, the specimen was cut to final dimensions of 2×2 mm^2 in-plane and 1.5 mm perpendicular to the basal planes. The side perpendicular to the basal planes (Fig. 1a) was mechanically polished down to 1 μm and then polished using 0.05 μm colloidal silica to obtain as smooth a finish as possible.

The specimen was mounted on a compression fixture which provided constraints from 3 sides, one side perpendicular and two sides parallel to the basal planes (Fig. S4). The sides parallel to the basal planes were constrained to avoid any lateral deformation. The *in situ* indentation was carried out using a Kammrath & Weiss tension-compression module inside a Tescan FERA-3 model GMH Focused Ion Beam Microscope. A cylindrical indenter with 1 mm radius was used, and the indentation was carried out at a crosshead speed of 0.5 μm/s giving a nominal strain rate of 0.25×10^{-3} s^{-1}. The indentation direction was parallel to the basal planes. *In situ* SEM imaging was done by intermittent interruption of the test to capture high resolution secondary electron (SE) images of the polished surface perpendicular to the basal planes. The intermittent stopping was done to capture any changes in the overall microstructure with changing indentation depth.

A sufficiently large Zr_2AlC single grain with the [0001] crystal orientation, located on a metallographic cross-section of the biphasic Zr_2AlC/ZrC ceramic, was selected for indentation by means of electron backscatter diffraction (EBSD; FEI Nova NanoSEM 450 Hikari XP EBSD detector). The procedure used to locate the Zr_2AlC grain is described in the supplementary material (see Fig. S5). Indenting the area of interest involved the formation of a square array of 5×5 indents at a spacing of 2 μm, using a load of 10 mN on a Hysitron TI 950 Triboindenter.

STEM analysis

The indented Zr_2AlC single grain was observed in a Zeiss 1540 EsB dual beam focused ion beam (FIB) SEM, and a cross-sectional thin foil was lifted out for scanning transmission electron microscopy (STEM) analysis. Electron microscopy work was done using a double-corrected FEI Titan^3 60–300 kV transmission electron microscope (TEM), equipped with a monochromated high brightness field emission gun (XFEG). High-resolution STEM images were acquired at 300 kV and ~10 pA beam current, using a beam convergence semi-angle of 21.5 mrad. High-angle annular dark field (HAADF) STEM images were recorded using a HAADF detector with an annular detection range of 46–200 mrad.

Atomistic simulations

All atomistic simulations were carried out within LAMMPS, the Large-scale Atomic/Molecular Massively Parallel Simulator (lammps.sandia.gov), an open source molecular dynamics code [22]. Visualizations of atomistic simulations were created with the open source software OVITO [23]. A bond-order potential for Ti_3AlC_2 (see Tables S1, S2 and Fig. S7 for details) was developed to describe interatomic interactions. All simulations used a timestep of 1 fs and ran within the NPT ensemble. An indentation simulation was performed on a $60 \times 1 \times 60$ nm^3 cell with a 10 nm radius cylindrical indenter. The indenter-MAX interactions were modeled with a simple repulsive force of the following form:

$$F(r) = -K(r - r_{tip})^2$$

where K is a specified force constant (10 eV/Å^3 in this case), r is the distance from an atom to the center of the indenter, and r_{tip} is the indenter radius. Periodic boundary conditions were applied to non-indentation directions, and a thin plane of atoms at the base of the indentation direction was held fixed to prevent the cell from moving. The cell was thermally equilibrated at 10 K for 50 ps prior to indentation at a rate of 10 m/s up to a maximum depth of 10 nm.

A uniaxial compression simulation was performed on a $20 \times 1 \times 40$ nm^3 cell, with the $[1\bar{2}10]$ direction being the compression axis. Periodic boundary conditions were applied in both the $[1\bar{2}10]$ and $[1\bar{1}00]$ directions while boundaries in the [0001] direction were treated as free surfaces. The cell was first thermally equilibrated at 300 K for 50 ps before uniaxial compression was performed to 20% strain at a rate of 10^8 s^{-1}. The same thermally equilibrated cell was also used for a simple shear simulation, in which shear strain was applied along the $[1\bar{2}10]$ direction at a rate of 10^8 s^{-1}.

Slip vector analysis

The slip vector metric, which was used to analyze atomistic simulations, is defined for each atom α as the following [24]:

$$\boldsymbol{s}^{\alpha} = -\frac{1}{n_s}\sum_{\beta \neq \alpha}^{n}\left(\boldsymbol{x}^{\alpha\beta} - \boldsymbol{X}^{\alpha\beta}\right)$$

where n is the number of nearest neighbors to atom α, n_s is the number of slipped neighbors, and $\boldsymbol{x}^{\alpha\beta}$ and $\boldsymbol{X}^{\alpha\beta}$ are the vector differences of atoms α and β in their current and reference positions respectively. The reference structure is simply taken as the unstrained one. In the MAX phase structure, nearest neighbors are defined differently for each atomic species: M atoms have both A and X nearest neighbors, A atoms have both M and A nearest neighbors, and X atoms have only M nearest neighbors. Slipped neighbors are defined as neighbors for which the vector difference is greater than a tolerance value – in this case, half the magnitude of partial slip ($a/2\sqrt{3}$). When the number of

slipped neighbors is zero, the slip vector is set to zero. The slip vector metric was validated for MAX phases by applying it to structures with known slip vectors (Fig. S8).

Results and discussion

Multiscale observations of kinking in single crystals

Compressing the basal planes of Cr_2AlC edge-on (Fig. S4) nucleated asymmetric delamination cracks parallel to the basal planes, together with RBs, beneath the indenter at an indentation depth of ~37μm (Fig. 1b, c). At a depth of ~71μm additional delamination cracks formed, which were slightly inclined to the loading axis and bridged by ligaments (Fig. 1d). At a depth of ~131μm, the ligaments between delamination cracks, in turn, buckled and kinked (Fig. 1e, f). In short, the SEM snapshots in Figs. 1 and S4 suggest that buckling and kinking occur simultaneously in the ligaments between the delamination cracks. Crucially, since most of these boundaries are not sharp, we label them RBs rather than KBs.

While valuable, *in situ* SEM observations cannot reveal atomic-scale mechanisms. To acquire the latter, a single grain was indented in polycrystalline Zr_2AlC, and an electron-transparent thin foil was extracted from the area beneath the indent. The indentation-induced Zr_2AlC deformation was then imaged using atomically resolved STEM. Fig. 2a is an overview of the region under the indent, showing a delamination crack parallel to the basal planes. It should be noted that even though the grain was loaded perpendicular to the basal planes, the material underwent compression parallel to the basal planes in the vicinity of the indenter tip. An atomic resolution image of the main delamination crack reveals a minute kink band (white dashed ellipse) with two distinct delamination cracks (white arrows) on either side (Fig. 2b). The kink band is three unit cells thick (Fig. 2c), while the delamination crack on the right of the kink band becomes atomically sharp close to its tip (Fig. S6). The importance of this atomic-scale kink band cannot be overemphasised since (i) it unequivocally demonstrates that atomic layers buckle, and (ii) it shows that at very high kink angles, the MX-layers do not only bend, but also fracture. Once they do, the boundary is no longer a reversible RB, but transforms into a KB.

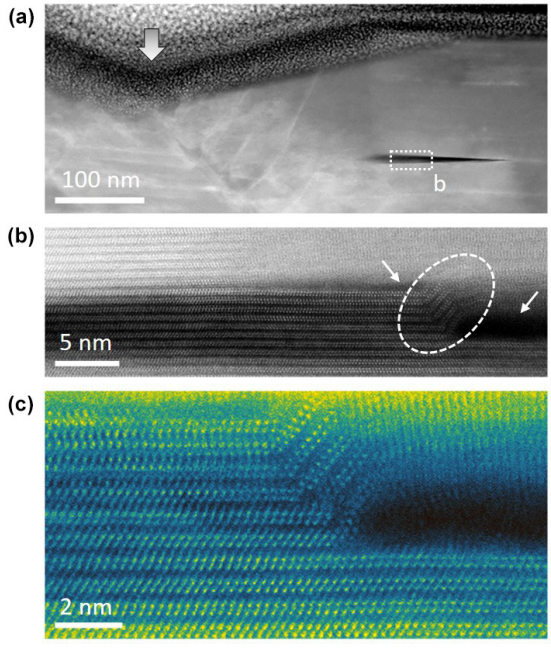

FIGURE 2

STEM imaging of indented Zr_2AlC single grain. (a) Overview of area underneath the indent with delamination at bottom right corner. (b) High magnification image of delamination reveals a minute kink band (ellipse) with delamination cracks on both sides (arrows). (c) Atomically resolved image of kink band. Note fracture of MX-layers.

The morphologies of the asymmetric delamination cracks and bands identified by STEM resemble those observed in Fig. 1. They are also morphologically identical to bands observed at the millimeter scale [25], implying that the mechanisms explored herein are operational over at least 6 orders of magnitude. To further understand kinking, we employ atomistic simulations.

Simulated indentation

Atomistic simulations of the MAX phases have previously been impossible because of the unavailability of accurate interatomic potentials. This work utilizes a newly developed bond-order potential for Ti_3AlC_2, which has been modified from a previous iteration [26] to better reflect deformation behavior. Like in Fig. 1, a 10 nm radius cylindrical indenter was loaded parallel to the basal planes. Snapshots from this simulation, up to indentation depths of 10 nm, are shown in Fig. 3 (also Supplementary Movie 1).

To better understand the nucleation of RBs we make use of the slip vector metric [24], a calculated atomic approximation of the Burgers vector (**b**). Analysis using **b** enables differentiation between atoms that have only undergone elastic deformation from those traversed by a lattice dislocation (see Fig. 3). At depths up to 4 nm, deformation is localized to the region directly beneath the indenter, where basal dislocations (BDs) nucleate at the contact surface and glide freely into the bulk (Fig. 3a). Slip occurs on basal planes subjected to the largest shear stress imposed by the cylindrical indenter (Fig. S9). The **b** of the red-colored atoms is a (~3.0 Å for Ti_3AlC_2), indicating basal plane portions traversed by perfect dislocations. The white-colored atoms, at the edges of these slip planes, correspond to a magnitude of partial slip, $a/\sqrt{3}$ (~1.7 Å for Ti_3AlC_2).

The presence of both perfect and partial slip regions indicates that basal slip is mediated by partial dislocations bounding stacking faults between them. As indentation progresses, the deformation becomes more delocalized, spreading to regions adjacent to the indenter. At a depth of 6 nm, RBs nucleate in these regions (Fig. 3b). At a depth of 8 nm, the RBs expand normal to the indentation direction, as slip is activated on more planes subjected to bending (Fig. 3c). At the maximum indentation depth of 10 nm, a kinked microstructure composed of numerous RBs, KBs, and delamination cracks develops (Fig. 3d). This microstructure is strikingly similar to the ones shown in Figs. 1 and 2. The boundaries are a mixture of RBs and KBs. An excellent example of a KB can be seen in Fig. 3g. The region denoted by the ellipse (magnified in inset) clearly shows fractured MX layers, whose morphology is uncannily similar to that shown in Fig. 2c.

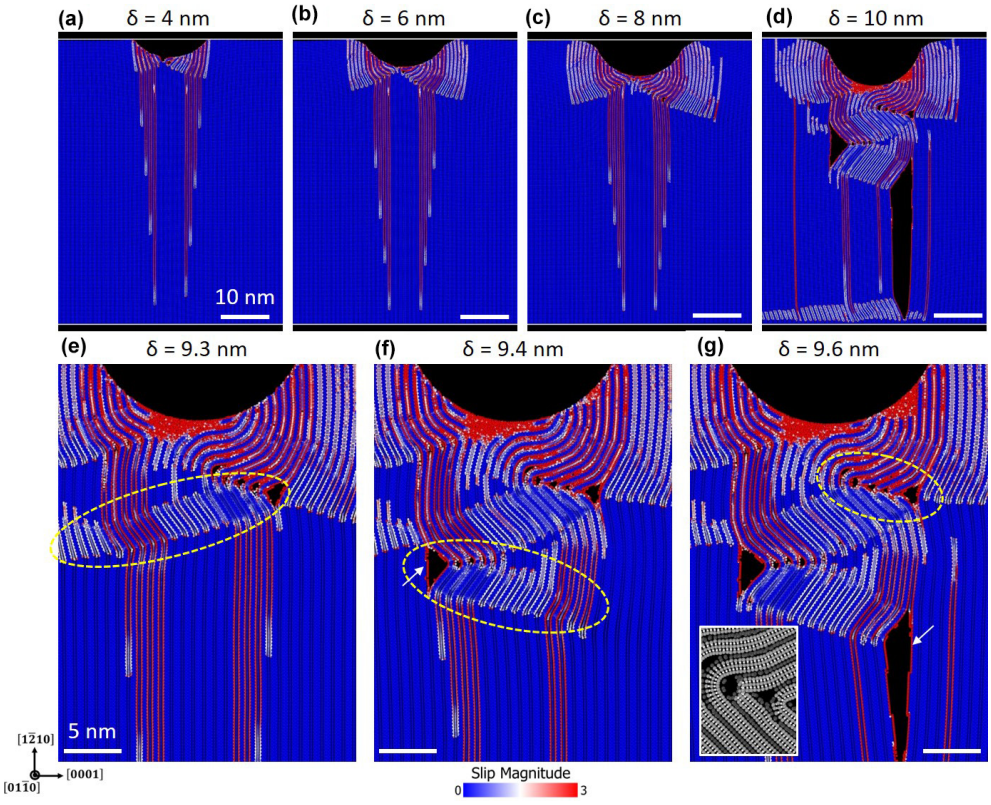

FIGURE 3

Simulated indentation of Ti_3AlC_2. (a) Dislocations nucleate from surface and glide into bulk. (b and c) RBs of opposite sign form on either side of indenter. (d) Complex kinked microstructure with delamination cracks forms. (e) Ripplocation band (ellipse) nucleation due to layer buckling. (f) Further layer bending nucleates another ripplocation band (ellipse) accompanied by a delamination (arrow). (g) Another delamination (arrow) emerges and propagates towards the simulation cell boundary. Here the MX layers fractured forming a KB (ellipse and inset). Values of δ denote indentation depths and atoms are colored according to their slip vector magnitude.

The formation of ripplocation and kink bands, and delamination cracks directly underneath the indenter is a process that involves several steps (Supplementary Movie 2). First, bending of multiple basal planes nucleates slip in a thin band of material, forming two RBs of opposite sign that define a ripplocation band (Fig. 3e). Next, bending in the opposite direction forms another ripplocation band of opposite orientation to the first and a delamination crack at their intersection (Fig. 3f). Note that, in the formation of these ripplocation bands, the majority of dislocations making up the RBs are generated during bending of the individual layers, however some pre-existing dislocations (seen in Supplementary Movie 2) are incorporated as well. Finally, another delamination crack forms on the other side of the ripplocation bands and propagates to the simulation cell boundary (Fig. 3g). Delamination cracks that appear after RB formation enable additional layer bending modes and the subsequent formation of complex kinked microstructures, similar to those observed in the *in situ* SEM experiments (Fig. 1). Despite the, at least, 3 orders of magnitude difference in the scales of Figs. 1 and 3, their similarity is a strong indication that we are dealing with a scale-independent phenomenon.

Kinking induced by uniaxial compression

Indentation produces complex strain states and deformations that are difficult to analyze. Therefore, a uniaxial atomistic simulation was carried out, snapshots of which are shown in Fig. 4 (also Supplementary Movies 3 and 4). After in-plane elastic deformation (not shown), a mode 2 buckle across the entire sample sets in (see Fig. 4a and inset). Interestingly, this buckling is similar to that proposed by Hess and Barrett [4].

At a strain (ε) of 0.1604 – an increase of 0.0001 over Fig. 4a – planes near the center of the simulation cell, where the shear stress is at a maximum, buckle locally resulting in two RBs denoted by green lines in Fig. 4e. Further increasing ε, by another 0.0001, separates the RBs from each other (Fig. 4c, f).

The localized buckling requires that layers slide relative to each other. Analysis of the relative motion of the MX- and A-layers shows, that between the RBs, the A-layers slip relative to the MX-layers. Burgers circuits around each RB (blue and orange lines in Fig. 4e, f) demonstrate that BD dipoles have nucleated. As such, the two circuits have equal and opposite $\mathbf{b}$ (blue and orange colored atoms in Fig. 4e, f). The magnitudes are $\sim a$ in Fig. 4e, in agreement with each circuit enclosing two partial dislocations, one on each M–A basal, or slip, plane. Basal slip is further evidenced by focusing on the red atoms; before kinking, there is zero disregistry between adjacent MX layers (Fig. 4d). As the ripplocation band forms, disregistry develops due to dislocation nucleation and glide between the MX- and A-layers (Fig. 4e, f and S10). As the ripplocation band grows, the BD dipoles glide away from each other, and the disregistry increases

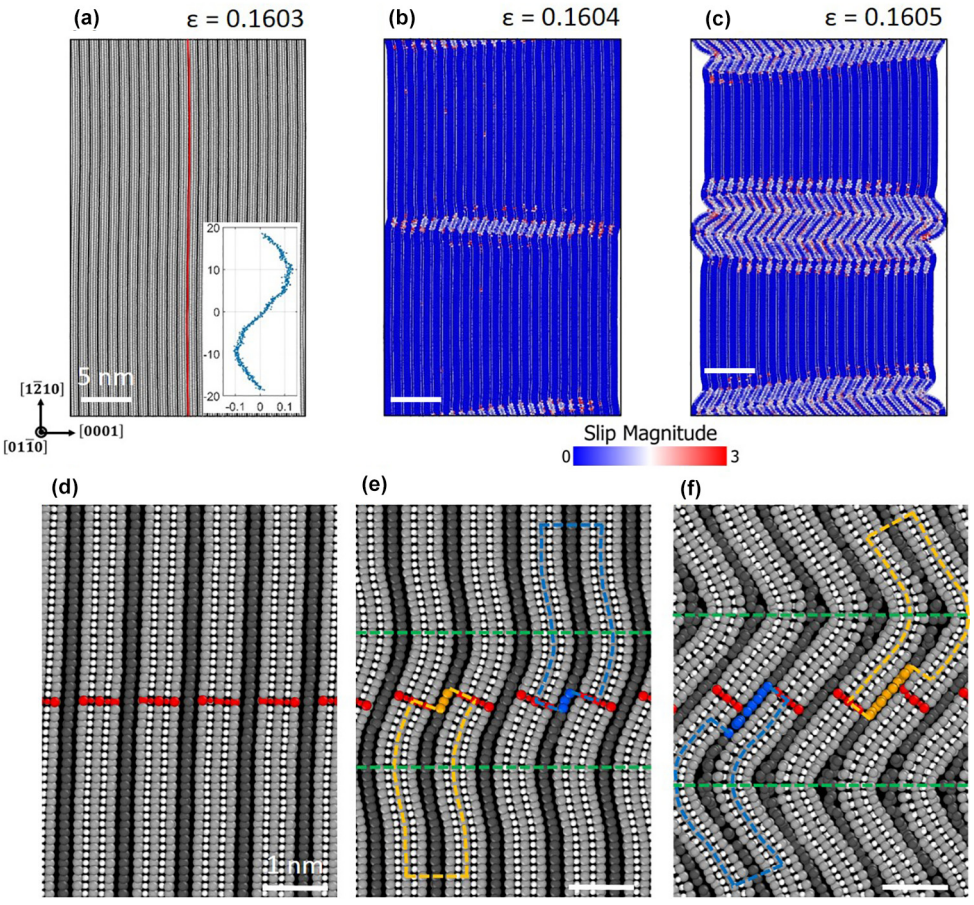

FIGURE 4

Uniaxial compression of Ti_3AlC_2. (a) Elastic layer buckling preceding kinking. Red line traces an A-layer in the center of the simulation cell with the inset depicting atomic positions along the length of the line. (b and c) RBs nucleate in regions of maximum shear and grow toward the free surfaces. Atoms are colored according to their slip vector magnitude. (d–f) Atomically resolved snapshots of ripplocation band formation corresponding, respectively, to (a–c). Atoms are colored by type: M – gray, A – black, X – white. Red colored atoms denote a column of M and X atoms with zero disregistry prior to ripplocation band formation. Blue and orange dotted lines and atoms denote Burgers circuits and vectors, respectively. Green dotted lines denote RBs.

as additional BDs are nucleated within the ripplocation band (Fig. 4f).

The BDs initially nucleate because the mode 2 buckle induces a non-zero resolved shear stress (RSS) near the sample's center. At a ~6° misorientation, the RSS is sufficient to overcome the slip barrier (Fig. S11). Note the slight misalignment of basal planes from vertical in Fig. 4d. Once BDs nucleate, the atomic planes around the BDs bend further, which in turn increases the RSS on neighboring slip planes, and a positive feedback loop develops. Thus, the entire process occurs quite rapidly. These comments notwithstanding, the slip and localized buckling cannot be separated; the latter cannot occur without the former. Paradoxically, that does not imply that BDs are necessary. In most macroscopic layered systems, such as composites, card or steel decks, etc. [1,10], interlayer slip is not mediated by BDs, but rather involves the frictional sliding of one layer relative to another. This BD feature is thus only applicable to LCSs where the slip planes have energetic surfaces (Fig. S7). Whether it applies to graphite and other van der Waals solids, where the energetic surface is comparatively flat, is an intriguing question that we are currently examining.

Before concluding, it is crucial to note that in the simulations the MX-layers only deform elastically, as evidenced by any Burgers circuit taken within a given MX-layer (Fig. S14), a crucial distinction between RBs and KBs. This does not, however, imply that the MX stress state does not change during the process. In Fig. 4d, e, the M–A–M distances remain more or less uniform. However, with further strain (Fig. 4f), the M−A−M distances between the RBs (i.e., location of red markers) shrink by ~20 %, while those at the RB cores expand by ~12 % resulting in considerable strain redistribution from, mainly, energetically more expensive in-plane bonds to cheaper out-of-plane bonds (Fig. S13). Similarly, the M–M bonds in the region between RBs are compressed by ≈ 1–8 % relative to the unloaded crystal. At the top of the MX layers, at the RB cores, the M–M in-plane bonds are stretched roughly 20 %; at the bottom of these layers, they are compressed by roughly 26 %. These strains are quite high and are responsible for the reversibility of the ripplocation bands.

Like in graphite [9], and presumably all other LCSs, this ε redistribution is the driving force for the entire process. Note that the gap opening between the M and A atoms also explains why the delaminations occur at the RBs and between the M- and A-

layers and not, for example, within the M- and X-layers. This is seen in Fig. 2 and in our previous work on mica [11]. Crucially, the increase in the M–A–M distances at the RB cores is another geometric imperative that occurs when parallel layers buckle. This open space, at least in our simulation, results in a loss of order of the A-atoms (Fig. S15). Whether this actually occurs in reality is an open question; it could well be an artifact of our atomistic model and warrants additional study.

Lastly, a perusal of the schematics shown in Fig. 4d–f, suggests that the MX-layers glide and elastically deform over the A-layers. In this respect, it is instructive to think of the A-layers as ball bearings for the elastically deforming MX-layers. Taking this analogy a step forward, it is useful in this context to imagine that the housing of these bearings, viz, the MX-layers, is not smooth but is pockmarked by a hexagonal pattern where the balls preferentially reside as they slip.

Conclusions

Here we leverage a combined experimental/computational study on kinking in the MAX phases to demonstrate that when the basal planes are effectively, or directly, compressively loaded edge-on, the response is first linear elastic (in-plane compressive strain accommodation) followed by elastic layer buckling. Further loading nucleates RBs. The leitmotiv of our ripplocation work to date is simple: atomic layers buckle like any other layers. This work once again confirms this important insight.

Our results confirm that LCSs deform by nucleating RBs at multiple scales; from the micrometric (Fig. 1) to the atomic (Figs. 2–4). The entire process would be impossible without interlayer slip between the MX- and A-layers, mediated here by the nucleation and glide of BD dipoles. Like for graphite, and presumably all LCSs, the driving force for the entire process is strain redistribution from energetically more expensive in-plane bonds to cheaper out-of-plane bonds. Notably this redistribution is confined to the region between RBs. At the RBs themselves, the elastic strains can be quite high indeed.

While our discovery deals with the MAX phases, given the very close resemblance of boundaries observed herein to those in other LCSs – such as mica, and other layered silicates, ice, graphite, etc. (see Fig. S1) – it is reasonable to assume it has universal validity. The best evidence for this idea is the plethora of ripplocation bands observed at the TEM level in deformed mica [11].

Additionally, the multiscale nature of kinking and its widespread occurrence accentuates its importance in the deformation behavior and associated strengthening/toughening of numerous natural and engineering materials. Taking into account that the MAX phases can be relatively tough ceramics and their fracture toughness is maximized in strongly textured samples, it is worthwhile studying the actual kinking contribution to their unique mechanical properties by systematically considering the loading direction relative to the crystal orientations favoring kinking. In this respect, this work not only provides an important step towards further unraveling the mechanical behavior of the MAX phases, but also towards the use of the herein gained insights into kinking to design innovative structural materials by using LCSs with a strong kinking propensity under application-specific loading regimes.

CRediT authorship contribution statement

G. Plummer: Methodology, Software, Validation, Investigation, Writing - original draft, Writing - review & editing. **H. Rathod:** Methodology, Investigation, Writing - original draft. **A. Srivastava:** Methodology, Investigation, Writing - review & editing. **M. Radovic:** Methodology, Investigation, Writing - review & editing. **T. Ouisse:** Methodology. **M. Yildizhan:** Methodology, Investigation. **P.O.Å. Persson:** Methodology, Investigation, Writing - original draft. **K. Lambrinou:** Methodology, Investigation, Writing - original draft, Writing - review & editing. **M.W. Barsoum:** Conceptualization, Writing - review & editing, Supervision. **G.J. Tucker:** Conceptualization, Writing - review & editing, Supervision.

Declaration of Competing Interest

The authors declare that they have no known competing financial interests or personal relationships that could have appeared to influence the work reported in this paper.

Acknowledgments

K.L. thanks T. Lapauw and J. Vleugels for the supply of Zr_2AlC and B. Tunca for the preparation and EBSD investigation of the Zr_2AlC sample prior to indentation. Work reported here was run on hardware supported by the High Performance Computing group at Colorado School of Mines.

Funding

G.P. acknowledges support through the CoorsTek Graduate Fellowship Program at Colorado School of Mines. G.J.T. is grateful for financial support through ARO Grant No. W911NF1910389. H.R. M.R. A.S. acknowledge support from the U.S. National Science Foundation through the DMREF program (Grant Nos. 1729335 and 1729350). M. W. B. acknowledges the support of NSF through CMMI program (Grant No. 1728041). P.O.Å.P. acknowledges the Swedish Research Council for funding under Grant Nos. 2016-04412, the Knut and Alice Wallenberg's Foundation for support of the electron microscopy laboratory in Linköping, and a project grant (KAW 2015.0043). P.O.Å.P. also acknowledges support from the Swedish Government Strategic Research Area in Materials Science on Functional Materials at Linköping University (Faculty Grant SFO-Mat-LiU No. 2009 00971).

Competing interests

The authors declare no competing interests.

Data and materials availability

All data is available in the main text or the supplementary materials.

Appendix A. Supplementary data

Supplementary data to this article can be found online at https://doi.org/10.1016/j.mattod.2020.11.014.

References

[1] G. Hunt, R. Butler, C. Budd, Phil. Trans. R. Soc. A. 370 (2012) 1723–1729.
[2] O. Mugge, Neues. Jahrb. Min. Geol. Paleont 1 (1898) 71–158.

[3] E. Orowan, Nature 149 (1942) 643–644.
[4] J.B. Hess, C.S. Barrett, Metals Trans. 185 (1949) 599–606.
[5] F.C. Frank, A.N. Stroh, Proc. Phys. Soc. B 65 (1952) 811–821.
[6] J. Gruber et al., Sci. Rep. 6 (2016) 1–8.
[7] M.W. Barsoum, G.J. Tucker, Scr. Mater.. 139 (2017) 166–172.
[8] J. Griggs et al., Acta Mater.. 131 (2017) 141–155.
[9] D. Freiberg, M.W. Barsoum, G.J. Tucker, Phys. Rev. Mater. 2 (2018) 053602.
[10] M.W. Barsoum et al., Phys. Rev. Mater. 3 (2019) 013602.
[11] J. Aslin et al., Nat. Commun. 10 (2019) 1–9.
[12] E.J. Freise, A. Kelly, Proc. Royal Soc. A 264 (1961) 269–276.
[13] I.A. Bell et al., Tectonophysics 127 (1986) 49–65.
[14] L. Farber, I. Levin, M.W. Barsoum, Philos. Mag. Lett. 79 (1999) 163–170.
[15] M. Higashi et al., Acta Mater.. 161 (2018) 161–170.
[16] T. Matsumoto et al., Acta Mater.. 151 (2018) 112–124.
[17] A.P. Rooney et al., Nat. Commun. 9 (2018) 1–7.
[18] M.W. Barsoum, Progr. Solid State Chem. 28 (2000) 201–281.
[19] M.W. Barsoum, M. Radovic, Annu. Rev. Mater. Res. 41 (1) (2011) 195–227.
[20] T. Ouisse et al., J. Cryst. Growth 384 (2013) 88–95.
[21] T. Lapauw et al., J. Eur. Ceram. Soc. 36 (2016) 1847–1853.
[22] S. Plimpton, J. Comput. Phys. 117 (1995) 1–19.
[23] A. Stukowski, Modell. Simul. Mater. Sci. Eng. 18 (2010) 015012.
[24] J.A. Zimmerman et al., Phys. Rev. Lett. 87 (2001) 165507.
[25] M.W. Barsoum, T. El-Raghy, Metall. Mater. Trans. A 30 (1999) 363–369.
[26] G. Plummer, G.J. Tucker, Phys. Rev. B 100 (2019) 214114.